Biomaterials Science

PAPER

View Article Online
View Journal | View Issue

Cite this: *Biomater. Sci.*, 2014, **2**, 1355

Advanced nanocomposites for bone regeneration

Kevin Baler,[a,b] Jordan P. Ball,[c] Zdravka Cankova,[a] Ryan A. Hoshi,[a] Guillermo A. Ameer*[a,b] and Josephine B. Allen*[c]

Received 21st April 2014,
Accepted 10th June 2014

DOI: 10.1039/c4bm00133h

www.rsc.org/biomaterialsscience

The field of orthopedic tissue engineering is quickly expanding with the development of novel materials and strategies designed for rapid bone regeneration. While autologous bone grafts continue to be the standard of care, drawbacks include donor-site morbidity and short tissue supplies. Herein we report a novel nanocomposite sponge composed of poly(1,8-octanediol-co-citrate) (POC) and the bioactive ceramic β-tricalcium phosphate (TCP). We show that these nanocomposite sponges can be used as a depot for bone-producing (a.k.a. osteogenic) growth factors. *In vitro* bioactivity is demonstrated by significant upregulation of osteogenic genes, osteopontin (~3 fold increase), osteocalcin (~22 fold increase), alkaline phosphatase (~10 fold increase), and transcription factor, RUNX2 (~5 fold increase) over basal expression levels in mesenchymal stem cells. *In vivo* osteogenicity and biocompatibility is demonstrated in a standard subcutaneous implant model in rat. Results show that the nanocomposite sponge supports complete cell infiltration, minimal adverse foreign body response, positive cellular proliferation, and cellular expression of osteogenic markers in subcutaneous tissue. The results shown herein are encouraging and support the use of this sponge for future bone tissue engineering efforts.

1. Introduction

Autologous bone grafts continue to be the standard of care to repair bone defects due to their intrinsic osteoconductivity, osteogenicity and osteoinductivity. However, their use is limited because of donor-site morbidity from the additional surgery and short supply of host tissue for grafting.[1–3] Consequently, the need to develop new orthobiologic materials to aid in the management of bone defects remains. As such, the field of orthopedic tissue engineering has been flooded in recent years with a variety of biomaterials proposed as bone grafts. The challenge is to ensure that there is a balance between the appropriate structural and mechanical requirements for the graft material and the necessary biological components to promote the growth of vascularized bone.

A major goal is to develop bone tissue alternatives for the treatment of bone defects from non-union fractures, traumatic bone injury, bone tumor resection, and spinal fusion cases where spontaneous bone restoration does not occur.[2] The diversity and complexity of these clinical problems requires the development of graft materials that are versatile, facilitating the customization of properties for the intended application. Bone grafts can be made from synthetic or naturally occurring materials.[4,5] Typical synthetic bone grafting materials come in a variety of physical forms such as liquids, powders, granules, putties, and porous rigid blocks to facilitate handling and delivery to the surgical site. Synthetic bone grafts or substitutes also come in a variety of compositions including bioactive ceramics, glasses, polymers, and polymer–ceramic composites.[6,7] There is increasing interest in developing synthetic grafts that are biologically active and will support bone regeneration but such devices are not commercially available to date.[6] Grafts derived from naturally occurring materials may consist of collagen-based scaffolds or demineralized bone tissue. These grafts represent a majority of off-the-shelf bone grafts on the market. More recently, there has been a significant clinical interest in the use of sponge-like orthobiologic grafts or matrices due to their ability to compress and readily expand into bone defects and the option to absorb marrow or cell suspensions into the sponge pore structure. All of the sponge-like bone grafts currently on the market are derived from demineralized allogeneic or xenogeneic bone that has been specially processed to maintain some degree of elasticity.[8,9] These materials have unpredictable performance and resorption characteristics due to the heterogenous tissue source and their long-term performance has yet to be evaluated. There are also reports in the literature on composite

[a]*Biomedical Engineering Department, Northwestern University, 2145 Sheridan Road, Evanston, IL 60208, USA. E-mail: g-ameer@northwestern.edu; Tel: +1 (847) 467-2992*
[b]*Chemistry of Life Processes Institute, Northwestern University, 2145 Sheridan Road, Evanston, IL 60208, USA*
[c]*Department of Materials Science and Engineering, University of Florida, Rhines Hall, Gainesville, FL 32611, USA. E-mail: jallen@mse.ufl.edu; Tel: +1 (352) 846-3328*

scaffolds that combine the properties of both synthetic elastomers and brittle materials.[10–12] While some of the results look promising, most approaches have limitations associated with biocompatibility, lack of tunability, lack of bioactivity, and toxicity.[13]

This report describes the characterization of a novel nanocomposite sponge that consists of a citric acid-based elastomer and bioceramic nanoparticles for orthopedic tissue engineering applications. The sponge consists of the elastomeric polymer, poly(1,8-octanediol-*co*-citrate) (POC) and β-tricalcium phosphate (β-TCP, $Ca_3(PO_4)_2$) nanoparticles. POC is a well-described biocompatible, elastomeric biomaterial that has been investigated by our group and others for a variety of tissue engineering applications.[14–19] The bioactive β-TCP is a ceramic material similar to the mineral found in native bone, hydroxyapatite ($Ca_{10}(PO_4)_6(OH)_2$). Both β-TCP and hydroxyapatite are calcium phosphate based minerals commonly found in nature with the hydroxyapatite mineral containing an additional hydroxide ion beyond the basic calcium phosphate block. While hydroxyapatite is found in human bone, β-TCP is more soluble than hydroxyapatite, thus making it more available for uptake by cells producing extracellular matrix during tissue regeneration.[20,21] However, the direct downside to this increased solubility, is that the accelerated release of Ca^{2+} and PO_4^{3-} ions will reduce the available surface area for bone cell proliferation.[22] While previous work explored the use of a POC/hydroxyapatite system, here we explored the inclusion of β-TCP into the POC elastomeric polymer as a strategy to enhance bone regeneration and limit the loss in available osteogenic surface area. This combination has been investigated due to the reported osteogenic properties of the constituents as well as an ideal balance between β-TCP solubility and the rate of new bone formation.[23–27] Overall, the POC/TCP sponge is degradable and shows great promise as a biologically active tissue engineering scaffold.

2. Experimental

2.1. Nanocomposite fabrication

Synthesis of poly(1,8-octanediol-*co*-citrate) (POC) was carried out as previously described.[28] All chemicals used in the synthesis were purchased from Sigma Aldrich (St. Louis, MO). Medical grade Beta Tricalcium phosphate nanocrystals (β-TCP) were purchased from Berkeley Advanced Biomaterials (San Leandro, CA). Briefly, equimolar amounts of citric acid and 1,8-octanediol were melted together at 160 °C while stirring. Once melted, the temperature was decreased to 140 °C and the mixture was stirred for approximately 1 hour to obtain the POC pre-polymer (pre-POC). The POC pre-polymer was purified to remove any unreacted monomers by precipitation in water and then freeze-dried. The purified pre-POC was mixed with sodium chloride (~250–300 μm diameter) and β-tricalcium phosphate (β-TCP) nanocrystals (100 nm diameter, specific surface area 50–70 $m^2\ g^{-1}$). The resulting composite was 85% sodium chloride and 15% POC/β-TCP. Of the 15% POC/β-TCP, we fabricated scaffolds with 40% TCP nanocrystal concentration. The composite was post polymerized at 80 °C for 3 days. The polymerized composites were then submerged in water to remove the 85% salt component which resulted in nanocomposite "sponge" with a theoretical overall porosity of 85%.

2.2. Nanocomposite characterization

Nanocomposite structure and mechanical properties. Assessments of the nanocomposite sponge include quantification of the overall scaffold porosity *via* mercury intrusion porosimetry. Pore size, distribution, and pore interconnectivity was assessed using ImageJ software. Qualitative evaluation of TCP nanocrystal distribution throughout the nanocomposites was performed *via* micro-computer topography (micro-CT) (Baxter Healthcare, Roundlake, IL). The nanocomposite scaffolds were imaged in 3 μm sections with approximately 500 sections used for analysis.

The compressive properties of the nanocomposite scaffolds were obtained using an Instron 5500 mechanical tester with a 500N load cell. Nanocomposite scaffolds were fabricated with 0%, 20%, and 40% TCP content and polymerized as previously described. Following the leaching out of the salt phase to create the porous construct, the scaffolds were cut into cubes (~125 mm^3) and subjected to compressive tests to obtain the compressive modulus (E_c). Six samples of each composition were evaluated.

In addition, following previously described methods; the compressive recovery ratio of the scaffolds was measured.[29,30] Porous scaffolds were cut into rectangular pieces 6 mm by 5 mm with a height of 4.5 mm. After 4 hours of soaking in PBS, samples were compressed to one fifth their height. The heights of the pieces were measured using electronic calipers before and after 2 min following 1 and 15 compressions using a TA.XT Plus Texture Analyzer (Texture Technologies, Scarsdale, NY) with a crosshead speed of 2 mm min^{-1}. Calculations were performed using eqn (1). Compressive moduli were also obtained from stress measurements while obtaining recovery ratio information with the Texture Analyzer.

$$\text{Recovery ratio} = \frac{h_f}{h_i} \times 100\% \quad (1)$$

Recovery ratio is calculated by dividing the final height (h_f) of a sample by its initial height (h_i), multiplied by 100%.

Nanocomposite degradation. The degradation characteristics of the 40% TCP nanocomposite sponge were assessed *in vitro via* dry weight measurements. Composite scaffolds were cut into cubes (125 mm^3) and incubated in phosphate buffered saline (PBS), pH 7.4 at 37 °C for up to 50 weeks under static conditions. To ensure the pH did not drop as the POC degraded, the pH was checked bi-weekly and the PBS was replaced as necessary. Samples were collected at 1, 5, 13, 31, and 50 weeks. At each time point a subset of samples was collected, rinsed extensively in deionized water to remove the degradation products, freeze dried, then weighed. Mass loss was obtained by comparing the initial weight with the final

weight at each time point. For each time point, six replicates were assessed.

Nanocomposite cell compatibility. To assess the cellular compatibility of the nanocomposites, both human osteoblast cells (HOst) and human umbilical vein endothelial cells (HUVEC) (Lonza, Walkersville, MD) were cultured within the scaffolds and cell proliferation was measured over 10 days. Briefly, the scaffolds were cut into cubes (125 mm^3), sterilized *via* ethylene oxide gas, and then hydrated in complete media corresponding to the specific cell type to be seeded. In this case, the complete media for the osteoblast was osteogenic growth media (OGM) (Lonza, Walkersville, MD). For the HUVEC cells, the media was composed of endothelial cell growth media 2 (EGM-2) (Lonza, Walkersville, MD). Both HUVEC and HOst cells were seeded at a density of ~50 000 cells per scaffold in a volume of ~25 μl per scaffold. The cells were allowed to attach to the scaffolds for 1 hour at 37 °C. After 1 hour, the culture wells were filled and the cell seeded scaffolds submerged in complete media for each cell type. The cells were cultured under static culture conditions for up to seven days. At various time points 1, 3, 5, and 7 days (n = 6) scaffolds were removed from culture, rinsed, then incubated for 20 minutes in 0.1% Triton-X solution to lyse the cells contained within the scaffold. The scaffolds were then subjected to sonication for 10 minutes to ensure complete lysis of the cells. The DNA was collected and quantified *via* Pico-green DNA assay kit (Life Technologies, Grand Island, NY).

Immobilization and release of bone morphogenic protein (BMP-2). The nanocomposites were loaded with BMP-2 solution in phosphate buffered saline (PBS) by adsorption. Prior to loading, BMP-2 was labeled with I-125 using the chloramine T/sodium iodine method.[31] Briefly, dried scaffolds were cut into cubes (125 mm^3), then incubated overnight at 37 °C in a solution of labeled BMP-2 (1 μg ml^{-1}). After overnight incubation, the scaffolds were rinsed with PBS, then freeze dried. BMP-2 immobilization onto the nanocomposite sponge was 220 ± 30 ng total and ~13 ng BMP-2 mg^{-1} scaffold dry weight, which is equivalent to approximately 20% loading efficiency. The loaded scaffolds were then submerged in 1 ml fresh PBS to monitor BMP-2 release. At various time points the supernatant was sampled and replaced with fresh PBS and the amount of BMP-2 released was quantified by radiodetection using a gamma counter. Direct radiodetection of the scaffolds was taken to quantify total protein incorporation.

Bioactivity of BMP-2 loaded nanocomposite. The osteogenic differentiation potential of the BMP-2-loaded nanocomposite scaffolds was used as a measure of bioactivity. Human mesenchymal stem cells (MSC) were cultured on the BMP-2-loaded nanocomposite scaffolds for 6 weeks in low glucose DMEM supplemented with 1% penicillin/streptomycin, 10% fetal bovine serum, and 4 mM L-glutamine (Life Technologies, Grand Island, NY). The media, which was changed every 3 days, was devoid of any additional soluble growth factors or cytokines that would direct stem cell differentiation. After 6 weeks in culture, the cells were lysed, and total RNA was extracted and purified using Aurum Total-RNA Mini-kit (Bio-Rad Laboratories, Hercules, CA). First-strand cDNAs were synthesized using 120 ng template with iScript cDNA Synthesis kits (Bio-Rad Laboratories, Hercules, CA). Gene expression was measured using real-time quantitative polymerase chain reaction (RT-qPCR). The expression of osteogenic genes alkaline phosphatase (ALPL), osteopontin (SPP1), and osteocalcin (BGLAP) as well as the osteogenic transcription factor, runt-related transcription factor 2 (RUNX2) were used as metrics of osteogenic differentiation in human mesenchymal stem cells. Glyceraldehyde 3-phosphate dehydrogenase (GAPDH) was used as a reference gene for data normalization. All genes observed, the primers used, and their corresponding NCBI reference sequences can be found in Table 1.

RT-qPCR consisting of 40 cycles of 95 °C for 10 s and 60 °C for 30 s, was carried out in a CFX Connect thermocycler (Bio-Rad Laboratories, Hercules, CA). 20 μL reactions were performed, in triplicate, using 1 μL (10 μM) each of forward and reverse primers, 6 μL nuclease-free water, 2 μL template, and 10 μL Advanced SYBR Green Supermix (Bio-Rad Laboratories, Hercules, CA). Primers were obtained from IDT DNA Technologies (Coralville, IA). RT-qPCR quality was assessed using gel electrophoresis to ensure amplicon length and melt curve analysis was performed to confirm appropriate amplification of the target gene without genomic DNA contamination.

2.3. *In vivo* biocompatibility evaluation

Experimental design. Porous poly(1,8-octanediol-*co*-citrate)-tricalcium phosphate (POC/β-TCP) disks (d = 1 cm, h = 0.5 cm)

Table 1 Genes used in osteogenic differentiation assessment

Gene	Symbol	NCBI ref. seq.	5′-Forward primer-3′ 5′-Reverse primer-3′
Alkaline phosphatase	ALPL	NM_001177520	GCTTCTTGTCTGTGTCACTCA ACCATTCCCACGTCTTCAC
Osteocalcin	BGLAP	NM_199173	GGTCTCTTCACTACCTCGCT CTCACACTCCTCGCCCTAT
Osteopontin	SPP1	NM_001040060	GTGATGTCCTCGTCTGTAGC CCCCACAGTAGACACATATGATG
Runt-related transcription factor 2	RUNX2	NM_004348	AGGCGGTCAGAGAACAAAC CTTCACAAATCCTCCCCAAGT
Glyceraldehyde 3-phosphate dehydrogenase	GAPDH	NM_002046.3	TCCACCACCCTGTTGCTGTA ACCACAGTCCATGCCATCAC

were implanted into the subcutaneous tissue of 6 Sprague-Dawley rats. The animals were split equally into two groups based on the type of implant that they received. The first group received POC/β-TCP disks and the second group received POC/β-TCP with immobilized BMP-2. Each animal received four identical implants (anterior right, anterior left, posterior right, posterior left). The amount of mineralization within the scaffold was quantified by histological staining at 4 weeks. Differences in cellular infiltration, quantitative fraction of total calcium deposits in the scaffold, and qualitative inflammation surrounding the different disks were assessed. Immunofluorescent staining for cell proliferation, as well as markers specific for osteogenic, inflammatory, and endothelial cells were used to qualitatively assess differentiation of infiltrating cells.

Animal surgery and tissue harvest. All animal procedures were approved by the Northwestern University Institutional Animal Care and Use Committee. Six female Sprague-Dawley rats (Harlan Laboratories, Inc.) weighing 150–175 g were used to evaluate the biocompatibility and osteogenic potential of POC/TCP composite scaffolds. Animals were anesthetized using the inhalant machine Impact 6 (Vetequip Inc., Pleasanton, CA). Isoflurane was administered at a concentration of 2% with an oxygen flow rate of 2 L min^{-1}. Following anesthesia, the backs of the animals were shaved and the incision sites were disinfected using alcohol and butadiene. Four incisions of approximately 1.5 cm in length were made at the implantation site and subcutaneous pockets were created by blunt dissection. POC/β-TCP disks (fabricated as described earlier) with and without immobilized BMP-2 (loaded as described earlier except with unlabeled BMP-2) were implanted in the subcutaneous pockets at a distance of 1–2 cm away from the incision site. The wounds were closed with surgical staples, which were removed 3 days post-operation. At the 4-week time point, the scaffolds and surrounding tissues were harvested from three animals. The explanted tissues were immediately snap-frozen, and stored at −80 °C until histologically evaluated.

Characterization of *in vivo* osteoinductivity. The explanted scaffolds and surrounding tissue were embedded in optimal cutting temperature compound (OCT, Tissue-Tek) after which the samples were cut in half, such that 5 μm thick serial cross-sections were obtained from the center of the explants and then out towards the edge. Sections were stained in one of three methods, with hematoxylin and eosin (H&E, Richard Allen Scientific, Kalamazoo, MI), with von Kossa (AMTS Inc., Lodi, CA), or with immunofluorescence for several different markers. The H&E and von Kossa staining were performed using standard protocols, following the manufacturer's specifications. For immunofluorescent staining, the sections were fixed in ice-cold methanol, then blocked in 5% fetal bovine serum (FBS) in phosphate buffered saline (1 PBS) + 0.1% Triton X100 for 30 minutes at room temperature. The sections were then probed overnight at 4 °C with antibodies specific for inflammatory marker, CD45 (Abcam, Cambridge, MA diluted 1 : 500), cell proliferation marker, Ki67 (Abcam, Cambridge, MA diluted 1 : 500), osteoblast marker, osteopontin (Abcam, Cambridge, MA diluted 1 : 250), and osteocalcin (Abcam, Cambridge, MA diluted 1 : 100), endothelial cell marker, CD31 (Abcam, Cambridge, MA dilution 1 : 200), and endothelial nitric oxide synthase (eNOS, Abcam, Cambridge, MA dilution 1 : 200). All antibodies were prepared in diluent solution composed of 5% FBS and 0.1% Triton X-100 in 1× PBS. Following overnight incubation, the sections were incubated with appropriate secondary antibodies for 1 hour at room temperature. Finally, the sections were rinsed with 1× PBS and mounted with DAPI containing mounting media for nucleus visualization. Sections were evaluated *via* standard light microcopy or fluorescence microscopy.

Explant imaging and analysis. Histological slides were viewed using a Nikon TE2000-U inverted light microscope (Nikon USA, Melville, NY). Digital images were obtained with an Olympus Qcolor3 digital camera (Olympus America Inc., Melville, NY) and analyzed with ImagePro Plus 5.0 software (Media Cybernetics, Silver Spring, MD). For each H&E cross-section, images were taken in 6–8 adjacent regions from the skin surface towards the core of the implant. ImageJ (NIH, Bethesda, MD) was used to stitch together the images in one composite per section. The same software was also used to image and stitch together the entire scaffold section as stained by von Kossa. A custom Java macro was written with ImageJ to count the ratio of darker calcium deposits (black) to the polymer fraction (tan) across the entire scaffold for each section.

Statistical analysis. One-way analysis of variance (ANOVA) was performed on three or more means. This was followed by a multiple comparison procedure to identify the groups that were significantly different. The pairwise comparisons were performed using critical values from the t distribution, after a Bonferroni adjustment to compensate for multiple comparisons. A $p < 0.05$ was considered to be significant.

3. Results and discussion

3.1. Nanocomposite fabrication

Structure and composition are important characteristics to consider in the development of any composite biomaterial system for use in tissue engineering. Specifically, scaffold architecture, porosity, pore size, as well as the distribution of the phases contained within the scaffold can affect the implant's performance. These scaffold characteristics are critical to promote the cellular processes at work during tissue formation and regeneration. Porous compressible composite scaffolds with up to 40% TCP nanocrystal concentration were successfully fabricated. The scaffolds were sponge-like and compressible with full recovery from deformation immediately upon release with no visible signs of rips, tears, or permanent deformation (Fig. 1a–c).

3.2. Nanocomposite characterization

Characterization of the nanocomposites included; morphological assessment, computer tomography, mercury intrusion

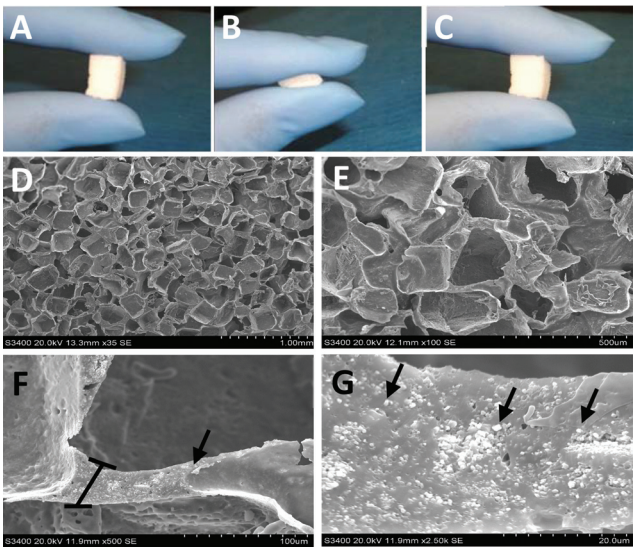

Fig. 1 Nanocomposite scaffold architecture. Manual compression of a representative POC/TCP nanocomposite scaffold demonstrating the ability of the scaffolds to recoil fully upon release of compressive force (A–C). Representative SEM images of nanocomposite scaffold showing pore architecture at 35× (D) and 100× (E). Representative SEM image of TCP nanocrystal distribution and orientation within the POC polymer wall in a 40% TCP composite at 500× (F) and 2500× (G). Arrows indicate TCP nanocrystals, which appear as white particles in the images and the bracket in image F indicates the cross section of the composite wall.

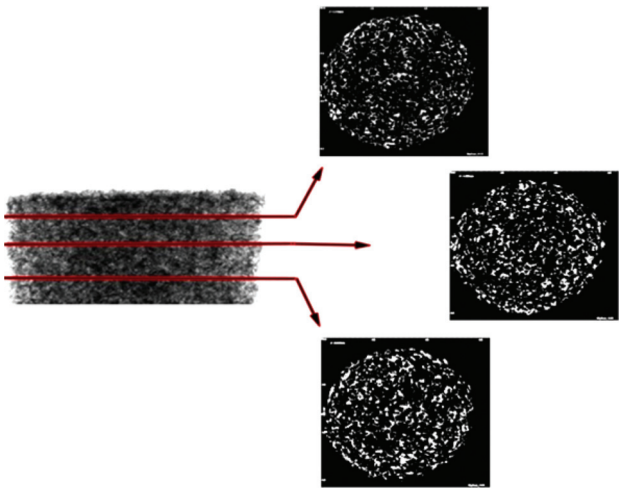

Fig. 2 Micro-CT scan of POC/TCP nanocomposite scaffolds. Representative cross sectional images of scaffolds showing distribution of 40% TCP (white) throughout scaffold. Black background represents POC and void space.

porosimetry, mechanical testing for compressive moduli and recovery from deformation, degradation studies, as well as quantitative analysis of microarchitecture. The micro architecture of the fabricated nanocomposites was observed visually *via* scanning electron microscopy (SEM). Representative images of the scaffolds are shown in Fig. 1d–g. The fabrication method used resulted in a homogenous pore size distribution (~250–300 μm) with interconnected pore structure. At high magnification, the distribution of the TCP nanocrystals becomes evident. The images show that the TCP nanocrystals are embedded in the POC polymer yet still exposed on the cell-contacting surface while some agglomeration between nanocrystals is apparent. Despite the agglomeration, the bioceramic TCP phase provides the attached cells with an osteogenic niche within the POC phase of the composite. Micro-CT scan images of the scaffolds confirm that the distribution of TCP nanocrystals is homogenous (Fig. 2). These data suggest that the incorporated bioceramic will be present throughout the degradation process, providing for the maintenance of osteogenic stimuli throughout the bone forming process, an important requirement of a bone graft.

Mechanical testing for compressive moduli reveals that the presence of the ceramic TCP nanocrystals within the walls of the POC increased the compressive moduli and thus the stiffness (Fig. 3a). With increasing TCP content (0–40%), the compressive modulus increased ($p < 0.05$). The POC/TCP composites achieve 100% recovery from compressive deformation following multiple compressive cycles (Fig. 3b). Regarding nanocomposite sponge degradation, over a period of 32 weeks the 40% TCP nanocomposites degraded significantly slower than POC scaffolds (14.7 ± 1.4% *vs.* 51.9 ± 6.5%, respectively). At a 50 week timepoint (not shown), the 40% TCP nanocomposite showed a 25% mass loss while the POC samples were completely degraded (Fig. 4). Collectively, the incorporation of β-TCP nanocrystals into the construct contributes to an increase in the overall mechanical properties of the scaffold as well as significantly reduces the rate of degradation, as compared to a scaffold composed of purely POC. We postulate that the inclusion of β-TCP within the composite acts to buffer the acidic degradation product of POC, thus reducing the degradation rate. This mechanism was shown to be evident in a study with polylactic glycolic acid (PLGA) as the composite polymer phase.[32]

Using mercury intrusion porosimetry, the actual sponge porosity was quantified and found to be 86.5%, which is in agreement with calculated values, validating our fabrication method to produce sponges of a desired porosity (data not shown). The characterization of the nanocomposites presented is very positive, and it should be noted that the structure and composition are quite tunable, due to the inherent flexibility of the polymeric POC phase, and the ability to control the nanocrystal ceramic phase. For example, the polymeric phase is a cross-linked network that may be modified by the selection of diol as well as increasing or decreasing the degree of cross-linking during polymerization. The modifications described have been shown to significantly affect the mechanical properties and the rate of degradation of the polymer phase, while still maintaining the scaffold biocompatibility.[28,33] Finally, the composite scaffolds can be embedded with increased or decreased concentration of the bioactive ceramic, β-TCP, thus further affecting the overall scaffold properties. The high compressibility and elastomeric nature of the POC/TCP sponges is also beneficial when it comes to the surgical handling of this material. More specifically, the inherent

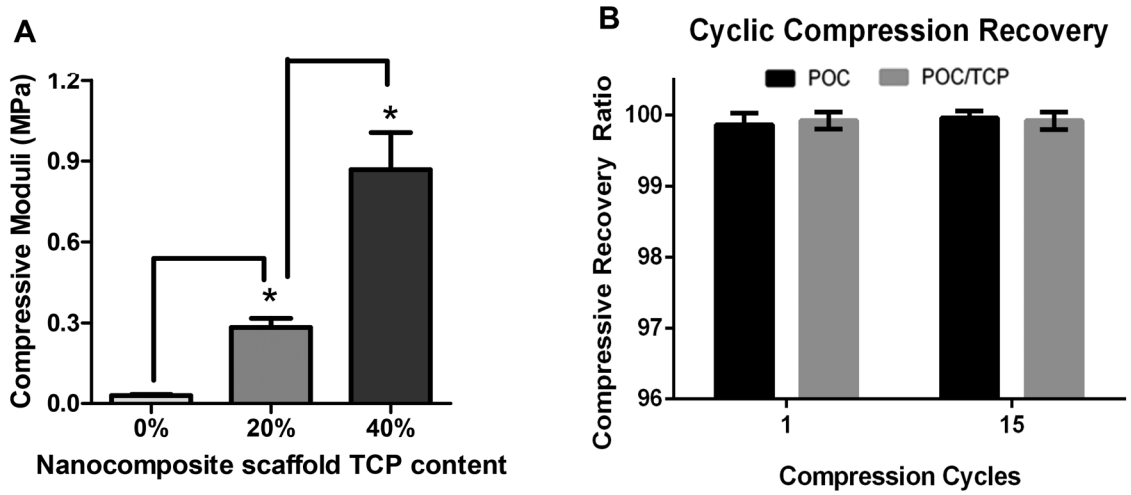

Fig. 3 Mechanical properties of nanocomposites. Data shown are the results of compressive testing of the porous POC/TCP scaffolds. (A) Compressive moduli from porous POC modified to contain 0, 20 and 40% TCP nanocrystals. Scaffolds of different TCP concentrations were fabricated in the same manner, to minimize architectural differences. All composites tested were 85% porous and 15% composite material with the indicated varying TCP concentrations. Data shown are Mean ± SD. $N \geq 6$. Asterisks (*) indicates statistically significant increase in modulus over the preceding lower concentration. (B) Percent recovery of a POC only scaffold compared to a POC scaffold containing 40% TCP after 1 and 15 compression cycles. Data are Mean ± SD.

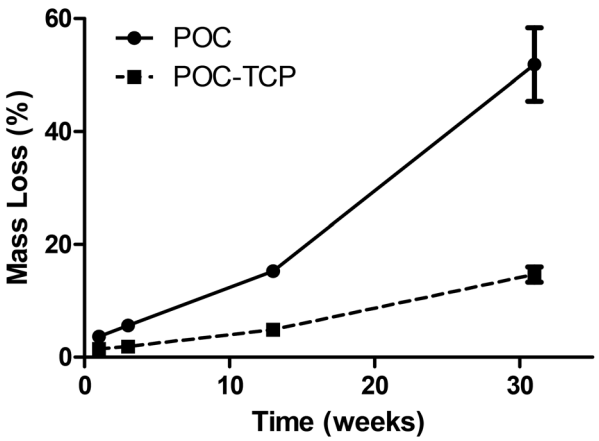

Fig. 4 *In vitro* degradation of nanocomposite scaffolds over 32 weeks in PBS at 37 °C. Solid line represents the degradation kinetic of porous POC scaffold without the addition of TCP nanocrystals. The dotted line represents the degradation kinetics of the porous POC with 40% TCP nanocomposite scaffold. Data shown are percent mass loss over the initial weight of each sample. Data are Mean ± SD (n = 4 samples for each time point).

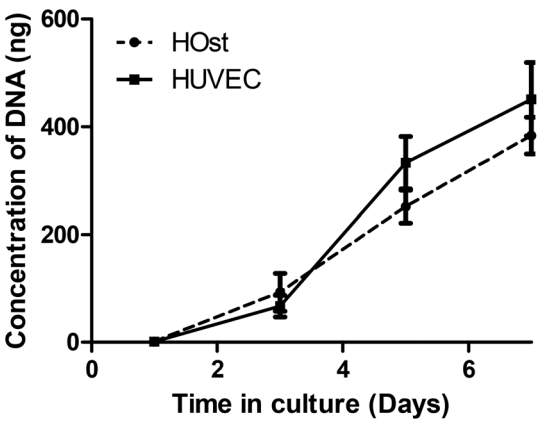

Fig. 5 POC/TCP nanocomposite scaffold biocompatibility as measured by proliferation of primary cells types, HUVEC and HOst over 7 days. Data shown are Mean ± SD, with n = 6 for each time point.

challenges of handling the brittle ceramic β-TCP are avoided by the addition of the elastomeric polymer. This along with recovery ratio testing demonstrates that even if compression of the scaffold is necessary for implantation, it is expected to regain its original shape. Also advantageous from a clinical standpoint is that this material can be easily cut into any desired size or shape during surgery to match a specific bone defect.

3.3. *In vitro* evaluation of cell compatibility

Cell compatibility studies were conducted with the POC/TCP nanocomposite scaffolds. Cell proliferation over 7 days in culture was measured for both primary human osteoblast cells (HOst) and human umbilical vein endothelial cells (HUVEC) (Fig. 5). There was an increase in the DNA content isolated from the scaffolds at each time point. The results show that the POC/TCP nanocomposite sponge supports the attachment and proliferation of bone osteoblast and vascular endothelial cells over 7 days, processes that are important to the generation of vascularized bone. In addition, the overall rate of proliferation of both cell types was consistent over the course of the experiment. To allow for complete restitution of a bone defect, a bone graft should not only be resorbable but support the replacement of the cellular constituents of newly formed bone.[34,35] Therefore, of great importance for this study is the ability of this nanocomposite construct to support bone and vascular cell infiltration and proliferation, which ultimately

leads to bone formation and the assembly of a vascular network. These results are not surprising since POC is known to be very conducive to the attachment and growth of several different cell phenotypes including osteoblasts, chondrocytes, and bone marrow derived mesenchymal stem cells.[18,36,37] Finally, in contrast to many other polymeric and ceramic scaffold designs, the POC/TCP nanocomposites were not coated or modified in any way to enhance cell attachment and proliferation, such as through the use of adhesion peptides, or proteins such as fibronectin, simplifying manufacture and regulatory path.

3.4. BMP-2 release from nanocomposites and bioactivity assessments

Growth factor release kinetics. In addition to supporting osteoblast and endothelial cell proliferative processes, we assessed the ability of the sponge device to promote bone marrow derived mesenchymal stem cell (MSC) differentiation with and without the addition of the osteogenic growth factor, bone morphogenic protein-2 (BMP-2). To achieve this, we conducted experiments to assess the release kinetics and ultimately the bioactivity of the released and/or scaffold bound BMP-2. BMP-2 has been widely studied and has been show to promote bone formation in several model systems.[34,38,39] Our data show that once labeled with radioactive iodine, we are able to accurately monitor the process of BMP-2 loading and subsequent release. The data show that we are able to incorporate approximately 250 ng of BMP-2 into our scaffolds (12 ng BMP-2 mg^{-1} of scaffold) (data not shown). Analysis of the BMP-2 release profile for up to 21 days from the nanocomposite shows that there is an initial (within 24 h) burst release of BMP-2 from the scaffolds, but significantly less BMP-2 released thereafter (Fig. 6). This initial burst release of BMP-2 is likely due to the fact that the BMP-2 was only physically adsorbed and not covalently cross linked onto the nanocomposite surface. These data demonstrate that the POC/TCP nanocomposites are able to sequester BMP-2, as demonstrated by the low levels of BMP-2 release from the loaded scaffolds over time. This sequestration is likely due to the affinity of calcium phosphates to electrostatically bind BMP-2.[34] The implication of these findings is very positive, in that the nanocomposite construct will maintain its osteogenic properties from both bioactive TCP as well as the loaded growth factor over the duration of bone formation.

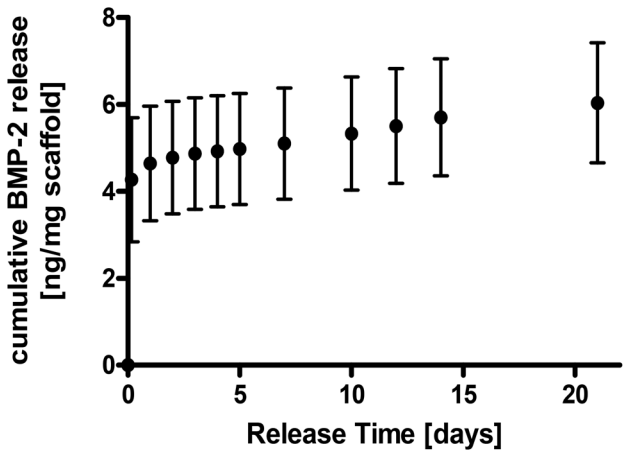

Fig. 6 Growth factor release kinetics from nanocomposite scaffolds. Cumulative release of BMP-2 from nanocomposite scaffolds was quantified over 21 days. Data are normalized to the weight (mg) of the scaffold prior to loading with BMP-2. Data are Mean ± SD ($n \geq 3$).

Bioactivity of BMP-2 growth factor loaded nanocomposites. The major challenge associated with the use of growth factors lies not only in their delivery but also in the amount required and maintenance of biological activity. BMP-2 is a known agonist to promote mesenchymal stem cell differentiation down an osteogenic pathway. To assess the bioactivity of growth factor loaded nanocomposites, osteogenic differentiation of adult bone marrow derived mesenchymal stem cells (MSCs) was measured by assessing changes in gene expression. Mesenchymal stem cells are multi-potent cells, able to differentiate into a variety of cell types, including osteoblast cells. This pathway of differentiation and the role of MSCs in the field of orthopedic tissue engineering has been extensively characterized and is the subject of several very thorough review articles.[40,41] Differentiation is often assessed on a genetic level, by evaluating changes in the stem cells gene expression to include osteogenic genes and transcription factors. As such, utilizing gene expression to determine the effectiveness of the POC/TCP sponge's ability to deliver bioactive BMP-2 is a very relevant metric. After being cultured for 6 weeks in basal media devoid of any additional soluble osteogenic growth factors, gene expression data show that the BMP-2 loaded nanocomposite scaffolds, containing 40% TCP, promote osteogenic differentiation of mesenchymal stem cells. It is emphasized that these experiments were conducted under conditions of basal media devoid of any additional soluble osteogenic stimuli, beyond that of the nanocomposite scaffolds. Significant upregulation of osteogenic genes, osteopontin (~3 fold increase), osteocalcin (~22 fold increase), alkaline phosphatase (~10 fold increase), and transcription factor, RUNX2 (~5 fold increase) were observed relative to the expression levels of MSC prior to seeding on the constructs. As expected, we also measured upregulation of these osteogenic genes by cells cultured on the TCP-containing nanocomposites scaffolds, again in basal media devoid of soluble osteogenic factors. However, the addition of BMP-2 to the nanocomposites further stimulates osteogenic differentiation above that seen with the nanocomposites alone (Fig. 7a–d). The genes chosen for our study are commonly used to demonstrate osteogenesis.[42–45] For example, RUNX2 is directly related in the transcription of skeletal genes and osteoblast differentiation. ALPL is a common bone-related marker gene and is associated with osteogenesis. SPP1 and BGLAP are genes that encode for proteins secreted by osteoblasts during mineralization. In addition, osteopontin, or SPP1, is a protein found in the extracellular matrix of bone. Finally, osteocalcin (BGLAP) serves to regulate calcium ion concentrations in the development of bone tissue. Up-regulation of these genes of interest is an indicator of osteoblastic differentiation of the mesenchymal

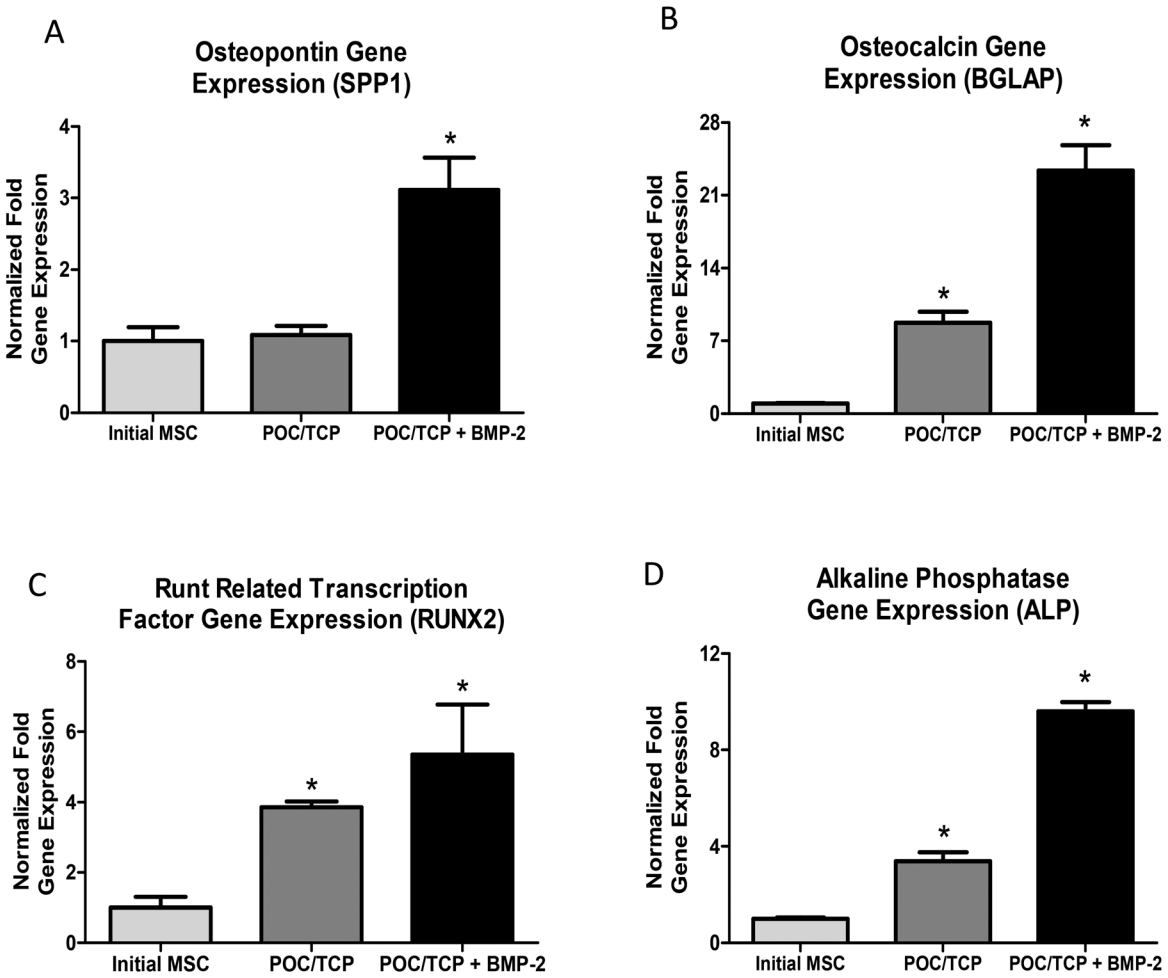

Fig. 7 Gene expression analysis of human mesenchymal stem cells cultured on BMP-2 loaded nanocomposites. The data above are normalized to GAPDH loading control to correct for any loading variations. The data are further normalized to the gene expression of mesenchymal stem cells prior to scaffold seeding. This "initial MSC" as noted above represents the baseline expression level of MSCs. Gene expression analysis of osteogenic genes, osteopontin (A), osteocalcin (B), runt related osteogenic transcription factor (C), and alkaline phosphatase (D). Data are Mean ± SD of normalized gene expression data (n = 6). (*) asterisk indicates a statistically significant increase in gene expression relative to the initial MSC gene expression.

stem cells cultured on our nanocomposite scaffolds. Interestingly, the POC/TCP nanocomposites demonstrated an intrinsic ability to upregulate osteogenic markers in the absence of exogenous growth factors when compared to a scaffold composed of POC alone. As expected, the inclusion of bioactive BMP-2 alongside TCP further promotes and enhances osteogenesis in MSCs over TCP alone but would add increased cost and complexity to a clinical product.

3.5. *In vivo* biocompatibility

Explant evaluation. To observe the recruitment and osteoinductive potential of the biomaterial in the absence of confounding factors such as the upregulation of BMP in the muscle pouch model, we used a common subcutaneous ectopic bone formation model.[46] Scaffolds with and without BMP-2 were implanted devoid of any cells. After 4 weeks *in vivo* in the subcutaneous pocket on the back of Sprague Daley rats, gross examination shows the nanocomposite scaffolds to be intact with no obvious signs of necrosis or inflammatory tissue (Fig. 8a–b). Histological evaluation of the explanted scaffolds *via* hematoxylin and eosin (H&E) show complete migration of cells throughout the scaffold by the 4-week time point. The large interconnected porous network is observed with cells attaching to the inner surfaces of the pores as well as filling in the empty spaces in the pore network (Fig. 8c). As expected, a thin fibrous capsule (FC) was observed in all scaffolds, and although present, this typical foreign body response did not interfere with the inward migration of cells into the scaffolds. These data are the first steps to demonstrating the ability of the nanocomposites to support full cell infiltration and localization *in vivo*, an important criterion for bone graft materials.

***In vivo* calcium content.** The percent mineralization of the implanted POC/β-TCP scaffolds with and without BMP-2 was 24.15% ± 9.07% and 33.33% ± 7.32% respectively (Fig. 9b). Representative images from each group are reproduced in

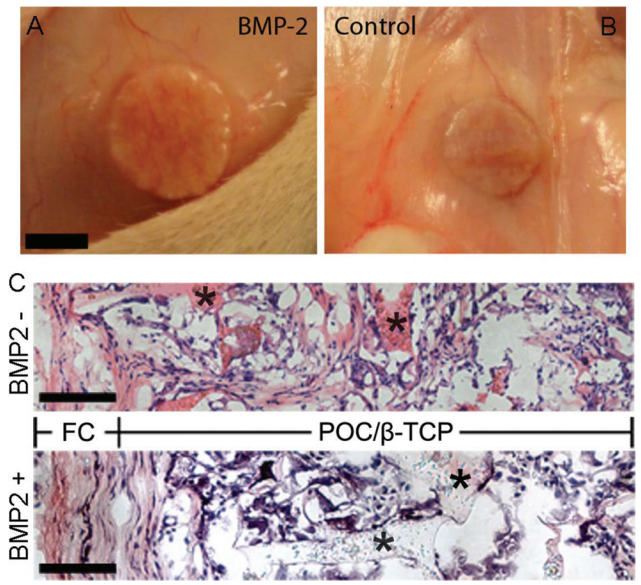

Fig. 8 Explant evaluation. Digital image of the scaffolds immediately prior to explant (A, B); histological staining of explanted scaffolds at 4 weeks (C). The hematoxylin and eosin (nuclei = purple, cytoplasm = pink, POC/β-TCP = pink or clear) stained sections are stitched together digitally from the dorsal (left) to the ventral (right) side of the implant which is also the direction of migrating cells into the scaffold (scale = 50 μm).

Fig. 9a showing 31.74% and 18.81% mineral content in the top (without BMP-2) and bottom (with BMP-2) respectively. Both implanted scaffolds showed a decrease in mineral content from the control scaffold that was not implanted *in vivo*. The differences between the three groups (non-implanted control, implanted POC/β-TCP with and without BMP-2) were significant ($p = 0.0035$). The results from posthoc pairwise comparison tests indicated that only the POC/β-TCP with BMP-2 was significantly lower than the non-implanted control ($p < 0.05$). These results suggest that there was resorption of the β-TCP, which was accelerated in the scaffold loaded with BMP-2. We know from our *in vitro* studies that the degradation of the POC/β-TCP at 4 weeks is <5%. As expected, we observed a greater decrease in calcium content *in vivo* due in part to scaffold degradation among other resorption mechanisms. The literature reports inconsistencies in the degree of β-TCP resorption *in vivo*. In a non-loading calvarial model, it was reported that β-TCP particles show minimal resorption.[47] According to other reports, the resorption of β-TCP particles increases significantly with the addition of BMP-2, findings that are consistent with our results.[34,38] This effect is likely due to the fact that osteoclastic bone resorption is increased in the presence of BMP-2.[48] Taken together, this may explain the observed differences between the resorption of the different scaffolds with and without BMP-2. Without the BMP-2, the measured decrease in total calcium content is possibly due solely to the degradation of the scaffold. With the BMP-2, the greater decrease in total calcium content is possibly due to both the scaffold degradation and additional resorption by migrating cells activated by the immobilized BMP-2.

***In vivo* characterization of nanocomposite biocompatibility and osteogenicity.** Since the implants were placed without an endogenous cell source into the subcutaneous pocket, which

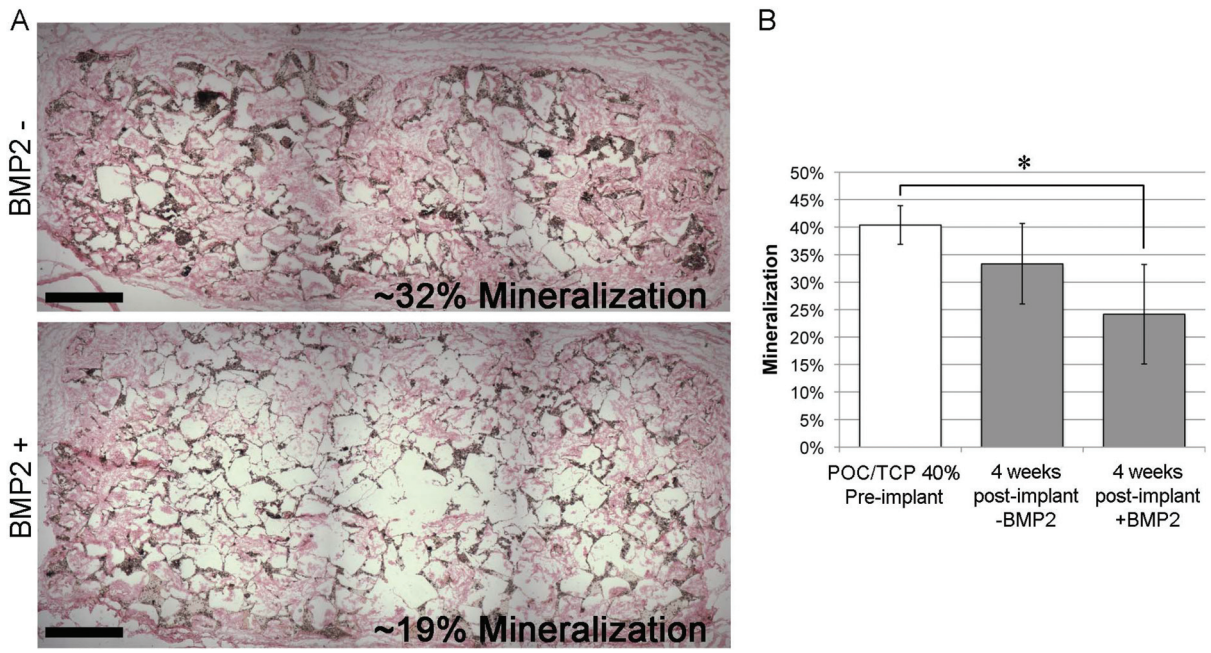

Fig. 9 Representative von Kossa stained POC/β-TCP scaffold. Representative digitally stitched images of entire sections stained by von Kossa (nuclei = pink, calcium deposits = black, POC/β-TCP polymer = tan, scale = 250 μm) (A). The top image represents POC/TCP scaffold not loaded with BMP-2, the bottom image represents POC/TCP scaffold loaded with BMP-2. (B) Percent mineralization of control scaffold, POC/β-TCP scaffold, and BMP-2 immobilized POC/β-TCP analyzed at 4 weeks after implantation. The differences between the three groups were significant ($p = 0.0035$). The BMP-2 + group was significantly different than the pre-implantation control ($p < 0.05$).

is theoretically devoid of naturally occurring bone-forming stem cells, it is not surprising to observe that no significant new bone grew and only calcium resorption occurred at the 4-week time point.[46,49] This model enabled us to observe the effect of the scaffold on migrating cells from the subcutaneous pocket, which was evaluated by immunofluorescence staining for several cell markers. We probed the tissue sections for Ki67 to identify proliferating cells, CD45 to identify inflammatory cells, as well as CD31 and eNOS, to identify endothelial cells. For this assessment, images were taken from the center of the scaffolds to investigate only the cells that had migrated into the material. At 4 weeks, samples were positive for Ki67 staining but negative for CD45 in both BMP-2 loaded and control scaffolds (Fig. 10a). The number of proliferating cells was consistent across all samples with less than 10% of cells positive for Ki67 consistent with non-tumorous cell proliferation. Both scaffolds, with and without immobilized BMP-2, showed positive CD31 staining (Fig. 10b, left) but results were inconsistent across different samples and locations (areas closer to the scaffold edge tended to have greater CD31 staining). Both images shown here were taken at the center of the implanted disk (Fig. 10b) and suggest ongoing migration of CD31 positive cells towards the scaffold center. The expression of eNOS was present and similar in both groups (Fig. 10b, right). The presence of CD31 and eNOS positive endothelial cells and the ability of the scaffold to support them without additional vascular growth factors is encouraging.

The osteogenic potential of the scaffold on the migrating and differentiating cells was evaluated by staining for osteocalcin and osteopontin. Osteocalcin and osteopontin are both markers associated with osteoblast cells. While osteopontin can stain positively for fibroblasts and other osteogenic cell types, osteocalcin is a very specific marker for osteoblasts.[50,51] Overall we observed highly specific osteocalcin staining and diffuse osteopontin staining in POC/β-TCP scaffolds with and without BMP-2 (Fig. 10c and d). Interestingly, while we expected osteoblasts or osteoclasts to be localized near the scaffold itself, we found that osteocalcin-positive cells tended to cluster together towards the center of scaffold pores. Osteopontin staining was more difficult to interpret due to

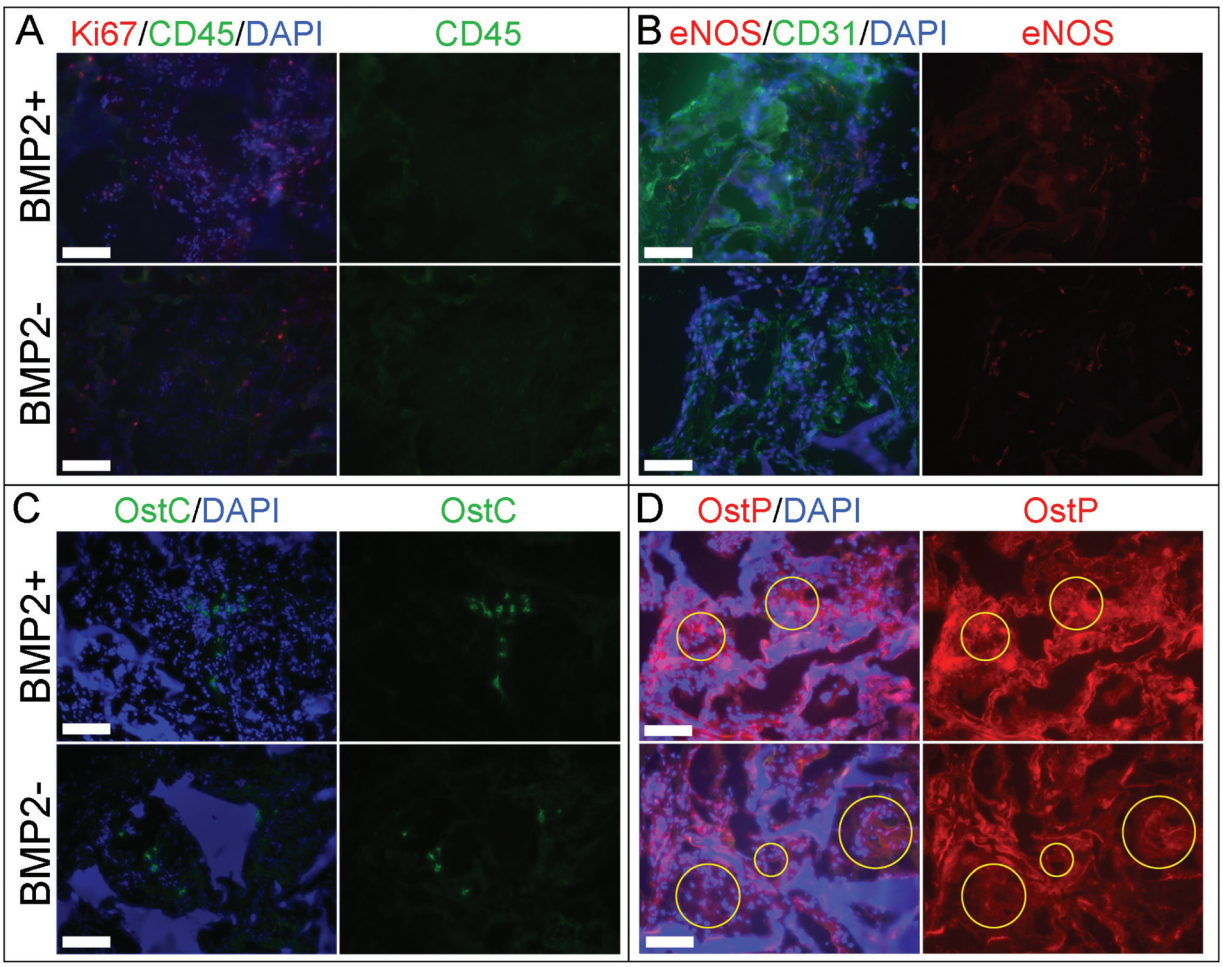

Fig. 10 Immunofluorescent staining of explanted scaffolds at 4 weeks. Ki67 (red) and CD45 (green) staining (A); eNOS (red) and CD31 (green) staining (B); osteocalcin (green) staining (C); osteopontin (red) staining with comparable polymer pore areas in yellow circles (D). In all image pairs, the composite images on the left show all the color channels (red, green, and blue) while the image on the right shows a single channel for (a) CD45, (b) eNOS, (c) osteocalcin, and (d) osteopontin for visual clarity. Scale = 100 μm.

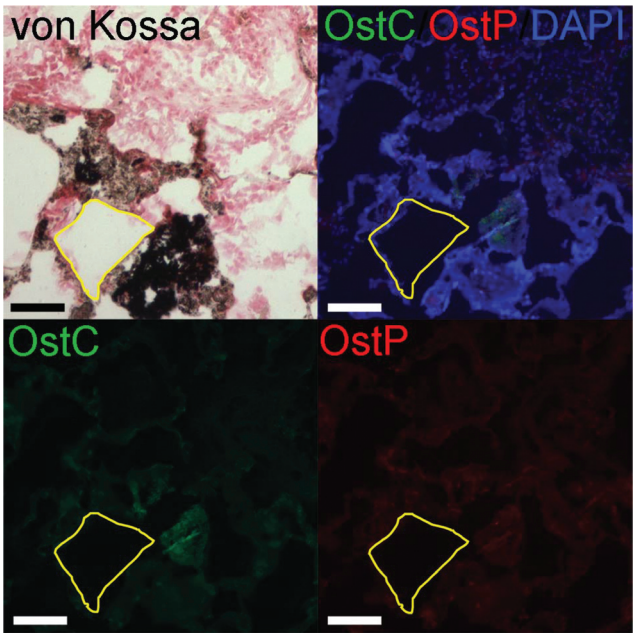

Fig. 11 von Kossa (top left) and immunofluorescent staining of serial sections. A yellow shape outlining a distinctive pore in the scaffold is drawn to assist spatial comparison between images. In the location of a large calcium deposit there is colocalization of osteocalcin (green) and little osteopontin (red). Scale = 150 μm.

diffuse red background staining and autofluorescence of POC which was consistent throughout the scaffolds and across samples. However, in the regions of interest (yellow circles) where there are cells and no polymer scaffold, elevated osteopontin staining is observed. To link these osteogenicity markers together, we attempted to perform serial sections of alternating von Kossa staining and immunofluorescent osteocalcin and osteopontin staining to provide qualitative co-localization for the cell markers and calcium deposits in a BMP-2 containing POC/β-TCP scaffold (Fig. 11). The yellow trapezoidal shape outlines a pore in the POC/β-TCP scaffold and is used as a distinctive feature near a calcium deposit to help the reader align the serial sections. While co-localization cannot be confirmed with the current data set, the presence of all these markers in the same pore near a large calcium deposit is encouraging. Adjacent to the longest side of the trapezoid, a dark calcium deposit was present with cell nuclei discernible at the top corner of the deposit. The cells in this area also stained positively for osteocalcin while osteopontin staining remained diffuse throughout the area.

The positive and highly specific osteocalcin staining is very promising due to the fact that these scaffolds were implanted without cells, therefore the observed osteoblasts are either locally differentiated cells or migratory osteogenic cells from the surrounding tissues. It is interesting to note that most of the osteoblasts are localized towards the center of the scaffold pores where there would be reduced contact with the embedded β-TCP in the scaffold walls. This suggests that a more ideal niche for osteoblasts is not directly on the scaffold surface but rather in the center of pores where there may be different mechanical forces, concentrations of BMP-2 or other factors that are not on the pore wall surface. Surprisingly, we found the presence of osteoblasts in the POC/β-TCP scaffolds without BMP-2 suggesting that the scaffold itself is sufficient to recruit the proper cell type in the absence of growth factors indicating its small but intrinsic osteogenic potential. Because of the subcutaneous model we selected, we know that the levels of endogenous BMP-2 due to injury from the surgery are minimal (in comparison to BMP-2 levels reported in the muscle pouch model) and not likely to affect the total concentration in the scaffold.[46] These *in vivo* results are consistent with our *in vitro* studies which show that mesenchymal stem cells had significant upregulation of osteopontin and osteocalcin after culturing them for 6 weeks on POC/β-TCP scaffolds. However, contrary to our *in vitro* results, our *in vivo* data do not show an enhancement in osteogenesis in scaffolds with immobilized, BMP-2. This may be due to either insufficient BMP-2 on the scaffold to see an effect *in vivo* where unlike *in vitro*, many additional factors can impact osteogenesis.

4. Conclusion

The field of orthopedic tissue engineering is growing at a rapid pace with the introduction of new materials that promote bone healing. Of particular interest within the field is the introduction of novel biocompatible materials with unique mechanical properties for easy delivery and to enhance bone regeneration. Herein we report a novel nanocomposite sponge that is compressible allowing for minimally invasive delivery and supports the immobilization and release of BMP-2. In addition, the *in vivo* data shows that the nanocomposite sponge supports complete cell infiltration, minimal adverse foreign body response, positive cellular proliferation and cellular expression of osteogenic markers when evaluated in subcutaneous tissue. The results support the further development and study of this sponge for use in bone tissue engineering.

Disclosures

None.

Acknowledgements

The authors would like to acknowledge Steven Strathmann for his work in obtaining the micro-CT data. The authors would also like to acknowledge Baxter-Northwestern Alliance for funding support for this project.

References

1 A. J. Salgado, O. P. Coutinho and R. L. Reis, *Macromol. Biosci.*, 2004, **4**(8), 743–765.
2 U. Kneser, D. J. Schaefer, E. Polykandriotis and R. E. Horch, *J. Cell. Mol. Med.*, 2006, **10**(1), 7–19.

3 C. Laurencin, Y. Khan and S. F. El-Amin, *Expert Rev. Med. Devices*, 2006, **3**(1), 49–57.
4 S. Bose, M. Roy and A. Bandyopadhyay, *Trends Biotechnol.*, 2012, **30**(10), 546–554.
5 T. Cordonnier, J. Sohier, P. Rosset and P. Layrolle, *Adv. Eng. Mater.*, 2011, **13**(5), B135–B150.
6 M. M. Stevens, *Mater. Today*, 2008, **11**(5), 18–25.
7 C. Ohtsuki, M. Kamitakahara and T. Miyazaki, *J. R. Soc. Interface*, 2009, **6**(Suppl 3), S349–S360.
8 T. T. Roberts and A. J. Rosenbaum, *Organogenesis*, 2012, **8**(4), 114–124.
9 A. S. Greenwald, S. D. Boden, V. M. Goldberg, Y. Khan, C. T. Laurencin and R. N. Rosier, *J. Bone Joint Surg. Am.*, 2001, **83-A**(Suppl 2 Pt 2), 98–103.
10 S. S. Kim, M. Sun Park, O. Jeon, C. Yong Choi and B. S. Kim, *Biomaterials*, 2006, **27**(8), 1399–1409.
11 S. Liao, W. Wang, M. Uo, S. Ohkawa, T. Akasaka, K. Tamura, F. Cui and F. Watari, *Biomaterials*, 2005, **26**(36), 7564–7571.
12 R. Zhang and P. X. Ma, *J. Biomed. Mater. Res.*, 1999, **44**(4), 446–455.
13 D. Sengupta and S. C. Heilshorn, *Tissue Eng., Part B*, 2010, **16**(3), 285–293.
14 H. Qiu, J. Yang, P. Kodali, J. Koh and G. A. Ameer, *Biomaterials*, 2006, **27**(34), 5845–5854.
15 D. Motlagh, J. Allen, R. Hoshi, J. Yang, K. Lui and G. Ameer, *J. Biomed. Mater. Res., Part A*, 2007, **82**(4), 907–916.
16 J. Yang, D. Motlagh, A. R. Webb and G. A. Ameer, *Tissue Eng.*, 2005, **11**(11–12), 1876–1886.
17 E. J. Chung, P. Kodali, W. Laskin, J. L. Koh and G. A. Ameer, *J. Mater. Sci. Mater. Med.*, 2011, **22**(9), 2131–2138.
18 C. G. Jeong, H. Zhang and S. J. Hollister, *Acta Biomater.*, 2011, **7**(2), 505–514.
19 M. P. Prabhakaran, A. S. Nair, D. Kai and S. Ramakrishna, *Biopolymers*, 2012, **97**(7), 529–538.
20 C. Knabe, F. C. Driessens, J. A. Planell, R. Gildenhaar, G. Berger, D. Reif, R. Fitzner, R. J. Radlanski and U. Gross, *J. Biomed. Mater. Res.*, 2000, **52**(3), 498–508.
21 S. Yamada, D. Heymann, J. M. Bouler and G. Daculsi, *Biomaterials*, 1997, **18**(15), 1037–1041.
22 T. W. Kim, Y. M. Park, D. H. Kim, H. H. Jin, K. K. Shin, J. S. Jung, H. C. Park and S. Y. Yoon, *Ceram. Int.*, 2012, **38**(3), 1965–1974.
23 H. Rojbani, M. Nyan, K. Ohya and S. Kasugai, *J. Biomed. Mater. Res., Part A*, 2011, **98**(4), 488–498.
24 E. R. Luvizuto, T. P. Queiroz, R. Margonar, S. R. Panzarini, E. Hochuli-Vieira, T. Okamoto and R. Okamoto, *J. Craniofac. Surg.*, 2012, **23**(5), e430–e433.
25 Y. Kang, S. Kim, M. Fahrenholtz, A. Khademhosseini and Y. Yang, *Acta Biomater.*, 2013, **9**(1), 4906–4915.
26 E. Kato, J. Lemler, K. Sakurai and M. Yamada, *Clin. Implant Dent. Relat. Res.*, 2014, **16**(2), 202–211.
27 B. Ozdemir and E. Okte, *J. Biomed. Mater. Res., Part B*, 2012, **100**(4), 976–983.
28 J. Yang, A. R. Webb, S. J. Pickerill, G. Hageman and G. A. Ameer, *Biomaterials*, 2006, **27**(9), 1889–1898.
29 Y. Kang, J. Yang, S. Khan, L. Anissian and G. A. Ameer, *J. Biomed. Mater. Res., Part A*, 2006, **77**(2), 331–339.
30 H. Kweon, M. K. Yoo, I. K. Park, T. H. Kim, H. C. Lee, H. S. Lee, J. S. Oh, T. Akaike and C. S. Cho, *Biomaterials*, 2003, **24**(5), 801–808.
31 G. C. Oliver Jr., B. M. Parker, D. L. Brasfield and C. W. Parker, *J. Clin. Invest.*, 1968, **47**(5), 1035–1042.
32 F. Yang, W. J. Cui, Z. Xiong, L. Liu, J. Z. Bei and S. G. Wang, *Polym. Degrad. Stab.*, 2006, **91**(12), 3065–3073.
33 A. R. Webb, B. D. Macrie, A. S. Ray, J. E. Russo, A. M. Siegel, M. R. Glucksberg and G. A. Ameer, *Ann. Biomed. Eng.*, 2007, **35**(8), 1357–1367.
34 U. Maus, S. Andereya, S. Gravius, J. A. Ohnsorge, C. Niedhart and C. H. Siebert, *J. Biomater. Appl.*, 2008, **22**(6), 559–576.
35 A. R. Vaccaro, *Orthopedics*, 2002, **25**(5 Suppl), s571–s578.
36 F. S. Shirazi, E. Moghaddam, M. Mehrali, A. A. Oshkour, H. S. Metselaar, N. A. Kadri, K. Zandi and N. A. Abu, *J. Biomed. Mater. Res., Part A*, 2013, DOI: 10.1002/jbm.a.35074.
37 A. K. Sharma, P. V. Hota, D. J. Matoka, N. J. Fuller, D. Jandali, H. Thaker, G. A. Ameer and E. Y. Cheng, *Biomaterials*, 2010, **31**(24), 6207–6217.
38 S. Dohzono, Y. Imai, H. Nakamura, S. Wakitani and K. Takaoka, *Clin. Orthop. Relat. Res.*, 2009, **467**(12), 3206–3212.
39 H. Schliephake, H. A. Weich, C. Dullin, R. Gruber and S. Frahse, *Biomaterials*, 2008, **29**(1), 103–110.
40 Z. Gamie, G. T. Tran, G. Vyzas, N. Korres, M. Heliotis, A. Mantalaris and E. Tsiridis, *Expert Opin. Biol. Ther.*, 2012, **12**(6), 713–729.
41 T. J. Heino and T. A. Hentunen, *Curr. Stem. Cell Res. Ther.*, 2008, **3**(2), 131–145.
42 J. E. Aubin, *J. Cell. Biochem.*, 1998, **72**(Issue Supplement 30–31), 73–82.
43 J. E. Aubin, *Rev. Endocr. Metab. Disord.*, 2001, **2**(1), 81–94.
44 I. Satokata, L. Ma, H. Ohshima, M. Bei, I. Woo, K. Nishizawa, T. Maeda, Y. Takano, M. Uchiyama, S. Heaney, H. Peters, Z. Q. Tang, R. Maxson and R. Maas, *Nat. Genet.*, 2000, **24**(4), 391–395.
45 R. S. Siffert, *J. Exp. Med.*, 1951, **93**(5), 415–426.
46 M. A. Scott, B. Levi, A. Askarinam, A. Nguyen, T. Rackohn, K. Ting, C. Soo and A. W. James, *Stem Cells Dev.*, 2012, **21**(5), 655–667.
47 J. Handschel, H. P. Wiesmann, U. Stratmann, J. Kleinheinz, U. Meyer and U. Joos, *Biomaterials*, 2002, **23**(7), 1689–1695.
48 H. Kaneko, T. Arakawa, H. Mano, T. Kaneda, A. Ogasawara, M. Nakagawa, Y. Toyama, Y. Yabe, M. Kumegawa and Y. Hakeda, *Bone*, 2000, **27**(4), 479–486.
49 E. C. Shors, *Orthop. Clin. North Am.*, 1999, **30**(4), 599–613.
50 N. Ashizawa, K. Graf, Y. S. Do, T. Nunohiro, C. M. Giachelli, W. P. Meehan, T. L. Tuan and W. A. Hsueh, *J. Clin. Invest.*, 1996, **98**(10), 2218–2227.
51 N. K. Lee, H. Sowa, E. Hinoi, M. Ferron, J. D. Ahn, C. Confavreux, R. Dacquin, P. J. Mee, M. D. Mckee, D. Y. Jung, Z. Zhang, J. K. Kim, F. Mauvais-Jarvis, P. Ducy and G. Karsenty, *Cell*, 2007, **130**(3), 456–469.

